A COMPARISON OF POLYAMIDE 11 MECHANICAL PROPERTIES BETWEEN LASER SINTERING AND TRADITIONAL MOLDING

David K. Leigh
Harvest Technologies, Belton, TX

ABSTRACT

Tensile properties of laser sintering grade Polyamide-11 are processed using laser sintering, compression molding, and injection molding and the resultant mechanical properties are reported. The primary contributor to the enhanced mechanical properties of injection molded specimens is a fully healed polymer melt with preferred polymer chain orientation. It can be shown that laser sintering and compression molding specimens have comparable to compression molding specimens Ultimate Tensile Strength (UTS) and Elongation at Break (EOB).

INTRODUCTION AND THEORY

1.1: LASER SINTERING

Additive manufacturing is a family of relatively new manufacturing processes utilizing integration techniques of digital solid models and the layer-by-layer addition of materials to create a three-dimensional solid. Selective Laser Sintering®, developed at The University of Texas at Austin, utilizes three major steps to create the three-dimensional solid.

1. The first step of the process is the computational evaluation of a solid model and a subsequent creation of a set of cross-sectional vector fields referred to as "slices." Each slice has a field of x-y vectors that represent the cross-sectional area of the model, with the aggregate total of these slices making up the complete 3-dimensional object. Each slice is prepared based upon a predetermined "layer thickness" which is typically 0.004 inches to 0.010 inches. Figure 1 illustrates the slicing algorithm process.

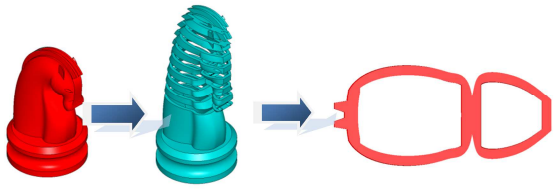

Figure 1: Illustration of CAD model slicing and an individual 2-D Slice

2. The second step of the process is to preheat a bed of powder, commonly a polyamide (nylon) material with an average particle size of 50 microns. Once the powder is heated to a sufficient temperature and the slice file is created, a directed energy beam (usually a CO_2 laser) scans the vector field on the prepared bed of powder. The fused layer reproduces the

cross-section generated by the vector field (or slice). A system schematic is illustrated in Figure 2.

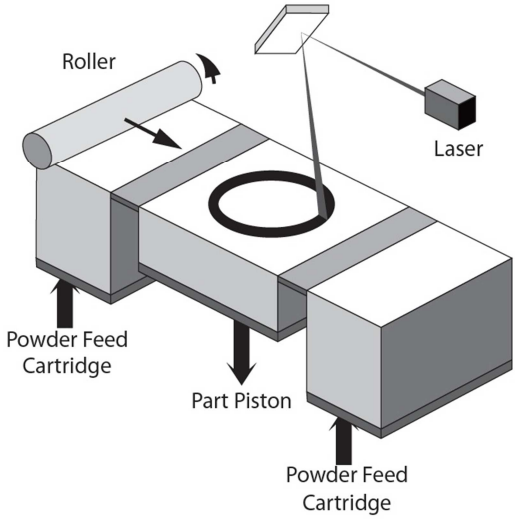

Figure 2: Schematic of Laser Sintering Process

3. The final step is to add raw material to the process so that subsequent "slices" can be fused together. A layer of powder equal to the predetermined layer thickness that was used during the slicing process is added, heated, and subsequently fused to prior layers to create a solid physical model, illustrated in Figure 3.

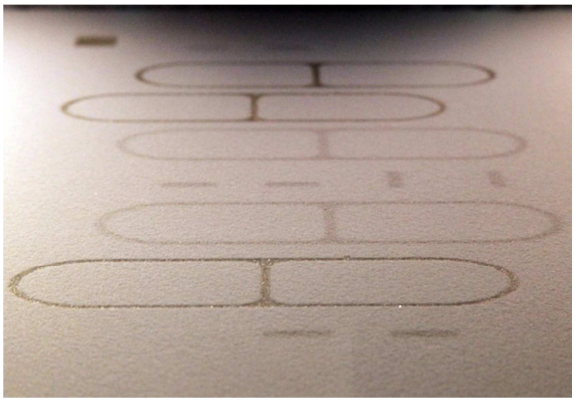

Figure 3: Photograph of powder bed being scanned. Darker areas have been scanned by the laser while the lighter sections are unaffected powder.

1.2: ADAPTATION OF LASER SINTERING FOR END-USE PARTS

The use of additive manufacturing and laser sintering in particular for low and medium volume production has become more important due to the cost savings associated with bypassing expensive tooling. (Ruffo, Tuck and Hague 2006) The laser sintering process has become more common in the production of end-use parts in various applications. This technique has allowed for streamlined design, decreased time to productize, minimal cost on engineering changes, and the ability to design for function rather than manufacturability. While there may be many benefits for certain applications, there are significant challenges that must be addressed prior to a broad acceptance of this technology. The key challenge is the limited amount of theoretical or

experimental science as well as detailed materials databases specific for the use of laser sintering as a manufacturing process. The use of laser sintered parts for end-use production has increased the scrutiny of the process but has channeled corporate funding towards the end of creating a stronger knowledge-base.

1.3: FORMATION OF LAYERS IN LASER SINTERING

Figure 4 is a graphical representation of the raw material powder bed. While the average particle size of the polyamide material is 50 microns, there is a distribution range of fine and coarse particles in a randomly packed bed. This powder bed is preheated to a point just below the melting temperature. If the particles are too hot they will pool, and there will be no distinction between the scanned area and the powder bed. If the particles are too cold, they will not have sufficient internal energy to allow for a full melt. In a region heated solely though laser energy will have significant dimensional distortion as the fused layer rapidly cools and shrinks due to the temperature gradient between the part and the surrounding powder bed. Part warping and in-build curl is created when the processed layer is fused to previous layers that have already undergone shrinkage. This adhesion will create residual stresses as the processed layer shrinks at a different rate than the previous layers.

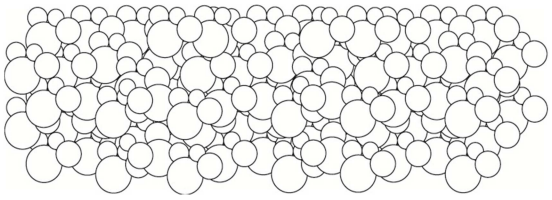

Figure 4: Cross Sectional Illustration of a Laser Sintering Powder Bed

Once the powder bed has been pre-heated, the laser will scan the subject cross-section using a field of x-y vectors at a prescribed speed, spacing, and laser power. These settings are optimized to yield an ideal melt pool such that there is sufficient energy to have a full melt without losing precision, seen in Figure 5. If the laser energy applied is too great, detail and precision are lost (analogous to writing on tissue paper with a large permanent marker). There is a corresponding depth of penetration directly proportional to the total energy applied.

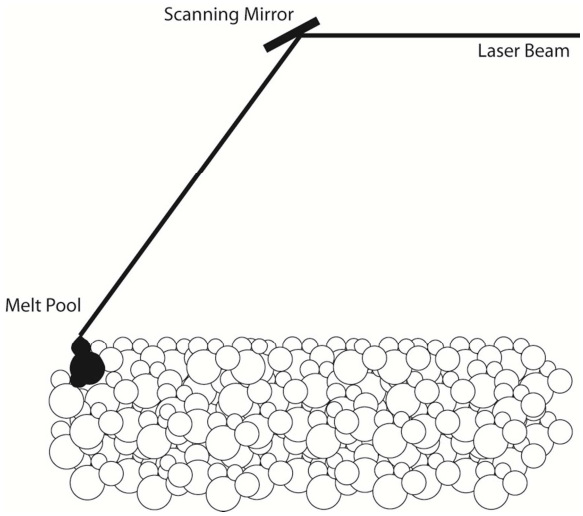

Figure 5: Melt Pool Generated on the Laser Sintered Powder Bed

1.4: PROCESS VARIABILITY AND PROCESS LIMITATIONS

A significant limitation to any layer-based additive manufacturing process is the anisotropic nature of the process. In this case, a single layer (typically 0.004" thick) is fused to the previous layer. The properties within this layer are fairly consistent, but the bond between layers is typically viewed as weak. Intralayer bonding is achieved as the laser passes across the pre-heated powder causing particles to melt and flow together in the creation of a molten region defined by the slice. Interlayer bonding is more challenging for three primary reasons: the previous layer that is being adhered to has had time to cool, the thin layer of powder that has been added serves as a thermal insulator and can inhibit laser penetration, and laser energy is absorbed and dissipated at a higher rate near the surface. This is discussed by Caulfield in "***Dependence of mechanical properties of polyamide components on build parameters in the SLS process"*** and illustrated in Figure 6. (Caulfield, McHugh and Lohfeld 2006) This work showed fracture lines in the x-y plane in z-axis oriented specimens followed the layer lines where the bond was weaker between layers.

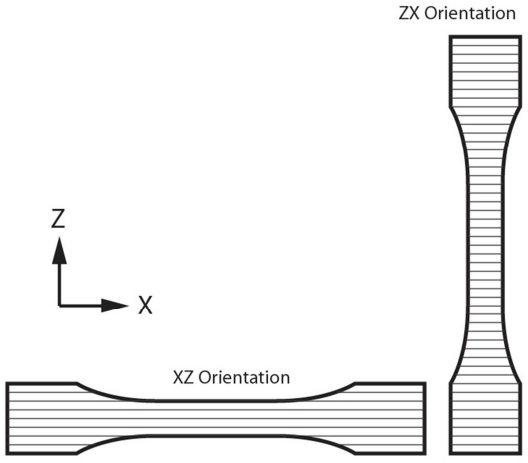

Figure 6: Part-build orientations. Black lines indicate layer interfaces.

As a quality assurance step during the production of end-use parts, it is common to quantify build performance through the placement of standard ASTM D638 tensile specimens oriented in the x-axis (left to right), y-axis (front to back), and z-axis (vertical build direction). It is generally observed that there is little to no variation between the x and y axes and that the z-axis will yield a significantly lower elongation at break (EOB) than the x and y axis specimens.

The primary cause of the lower mechanical properties in the z-axis can be attributed to layer-to-layer adhesion (interlayer bonding). Several papers have been dedicated to the characterization and optimization of the laser sintering process in relation to z-axis anisotropy. Several key factors that contribute to poor interlayer bonding (layer-to-layer adhesion):

- Large layer size – The powder insulates the thermal energy and prevents the energy of the beam from penetrating to the prior layer.
- Poor powder quality – Used powder will yield a high melt-flow and higher molecular weight. This is primarily caused through thermal aging and cross-linking of the polymer. The result of the high melt-flow is a polymer that is slow to melt with a high viscosity. The result is the creation of voids between layers.
- Poor thermal control – If the powder bed is processed in a way that the temperature is too low or is cooled at a high rate, it will inhibit the formation of a melt pool that penetrates the previous layer. The result can be weak layer-to-layer adhesion as well as dimensional distortions.
- Low laser energy – High scan speed, low laser power, and large spacing between scan vectors (scan spacing) can lower the overall laser energy delivered to the powder bed. This decreased energy will not yield sufficient energy to penetrate the current layer and create strong layer-to-layer adhesion.

1.5: PREVIOUS WORK ON PROCESS OPTIMIZATION AND CHARACTERIZATION

Laser sintering became a broadly used additive manufacturing process in the early 1990s with the introduction of Duraform® PA, a Polyamide 12 material. Christian Nelson published an article in 1995 speaking to the need for process and material optimization to improve part accuracy. (Nelson, McAlea and Gray 1995) The primary application of laser sintering in the early stages of development was functional prototypes and concept models with the chief competitor being 3D Systems™ Stereolithography (SL) process. While laser sintering held an edge over the SL process in material properties, the SL had become the de facto standard in prototyping and held an edge in accuracy. The conclusions that Mr. Nelson made at the time were:

- Use of better galvanometers to control the laser and scanners will increase accuracy and repeatability.
- Optimization of scanning parameters can improve surface finish, accuracy, and repeatability.
- Optimized powder particle distribution can yield surface finish comparable to those made with liquid based techniques.

With increased utilization of the laser sintering process in the 1990s, there became a focus on process optimization and repeatability in regards to the use and re-use of raw material. Poor accuracy, surface finish, and overall part quality were seen in parts being made with Duraform® PA due in large part to inconsistent raw material and a thermal degradation of the material. There were several schools of thought that were proposed to mitigate this issue:

- David Keith Leigh of Harvest Technologies developed work done to create a steady-state mixture of used and virgin based on quantified mechanical properties and qualified visual inspection of the parts. (Leigh and Gornet n.d.)
- Timothy J. Gornet of the University of Louisville developed work done on quantifying the melt flow rate and correlating this measurement to a usable standard. Virgin powder would be added to the powder feedstock based on a quantified melt flow reading. (Leigh and Gornet n.d.)
- John Choren proposed varying manufacturing parameters based on the powder age or thermal degradation. (Choren, et al. 2001)

Based on a paper written by Choren in 2001, it was noted that thermal processing parameters were stable but that laser power had to be increased over time. (Choren, et al. 2001) The mechanical properties achieved are shown in Figure 7 with the elongation at break absent from this data. In addition to this work, a 2008 paper by Yusoff showed the effects of powder degradation on surface finish. (Yusoff and Thomas 2008) These two published reports as well as work done by Leigh and Gornet illustrate the effect of powder melt flow (molten viscosity) on material properties, machine parameters, and part quality. (Leigh and Gornet n.d.)

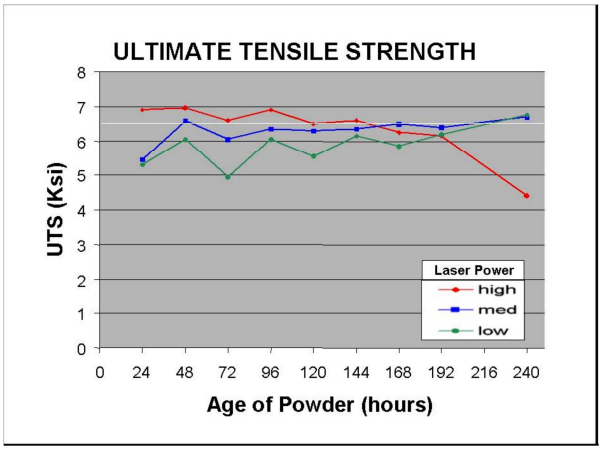

Figure 7: UTS Data taken from 2001 Choren powder life study. (Choren, et al. 2001)

Further research in quantifying the effect of powder melt and mechanical properties was performed by Majewski at the University of Loughborough in 2008. (Majewski, Zarringhalam and Hopkinson 2008) This article was able to determine both visually and with Differential Scanning Calorimitry (DSC) that there were two distinct melt peaks representing areas in the processed part that had not been fully melted. It was proposed that the Degree of Particle Melt (DPM) had an overall impact on mechanical properties. A key conclusion in this research was stated:

This work has shown that the percentage crystallinity of a two-phase SLS part, as calculated from a DSC chart, has an appreciable effect on the Tensile Strength and Elongation at Break, whereby a decrease in crystallinity leads to an increase in the mechanical property. (Majewski, Zarringhalam and Hopkinson 2008)

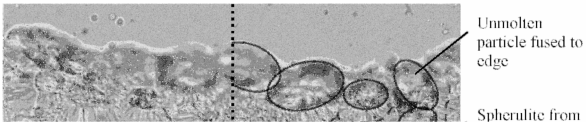

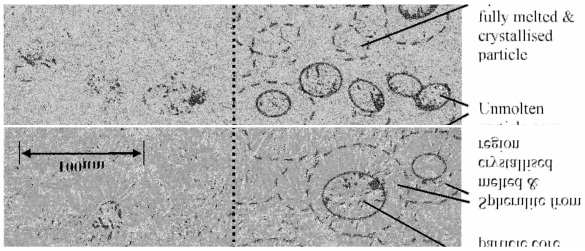

Figure 8: Laser Sintering Morphology taken from Particle Melt Study (Majewski, Zarringhalam and Hopkinson 2008)

In work that has yet to be published at the University of Louisville, Thomas L. Starr and Timothy J. Gornet have research that further helps characterize the correlation of process settings, material morphology, and resultant mechanical properties. Starr correlates the amount of energy that is delivered to the part bed during laser sintering (Energy Density) to the resultant material properties. The formula for energy density is shown in Equation 1 and a plot of Yield Stress and Elongation at Break are in Figures 9 and 10, respectively. (Starr, et al. 2008) The energy to melt is shown to be insufficient for optimized material properties and it is proposed that there is an effective Energy to Melt Ratio. This excess energy is necessary for stronger layer-to-layer adhesion. In addition, Gornet shows in separate work that the use of microtoming is a practical tool in analyzing laser sintering morphology. (Gornet 2010) Figure 11 shows a microtomed cross-section of a specimen with layer lines being apparent in both magnifications. Correlating these images with those from Majewski in Figure 8, it can be seen that the particles that are not fully melted are colinear in the photographs which is a result of the coplanar phenomenon of decreased energy density at the bottom of the sintered layer.

$$\textbf{Energy Density} = \frac{\boldsymbol{Laser\ Power}}{(\boldsymbol{Scan\ Spacing})(\boldsymbol{Scan\ Speed})(\boldsymbol{Layer\ Thickness})} \qquad \textbf{(Equation 1)}$$

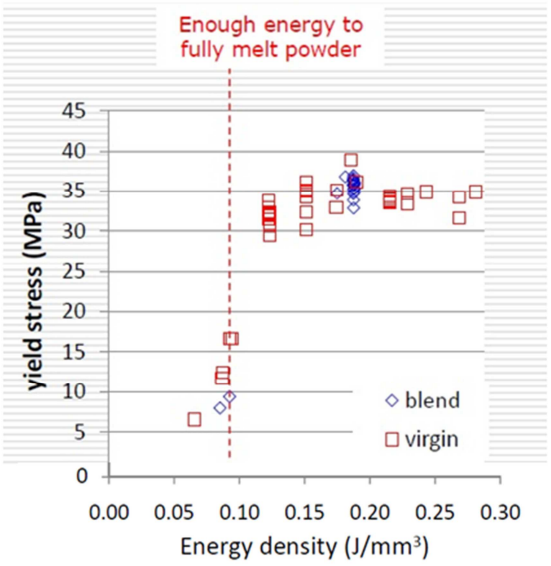

Figure 9: Plot of Yield Stress vs. Energy Density used from (Starr, et al. 2008).

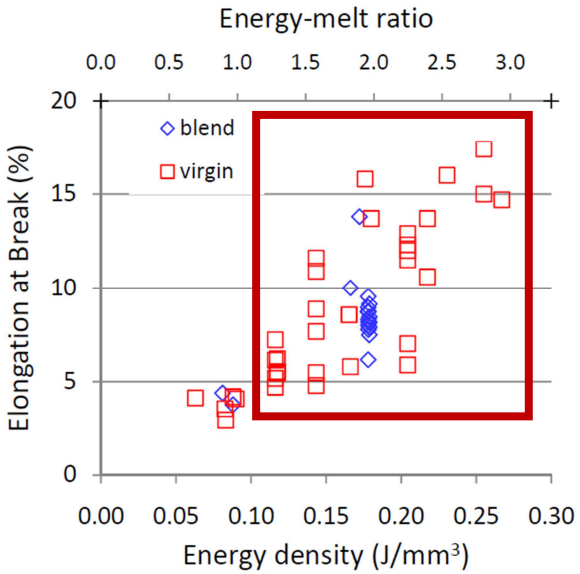

Figure 10: Plot of Elongation at Break vs. Energy Density used from (Starr, et al. 2008). There is no correlation between strength in Figure 9 that guarantees ductility.

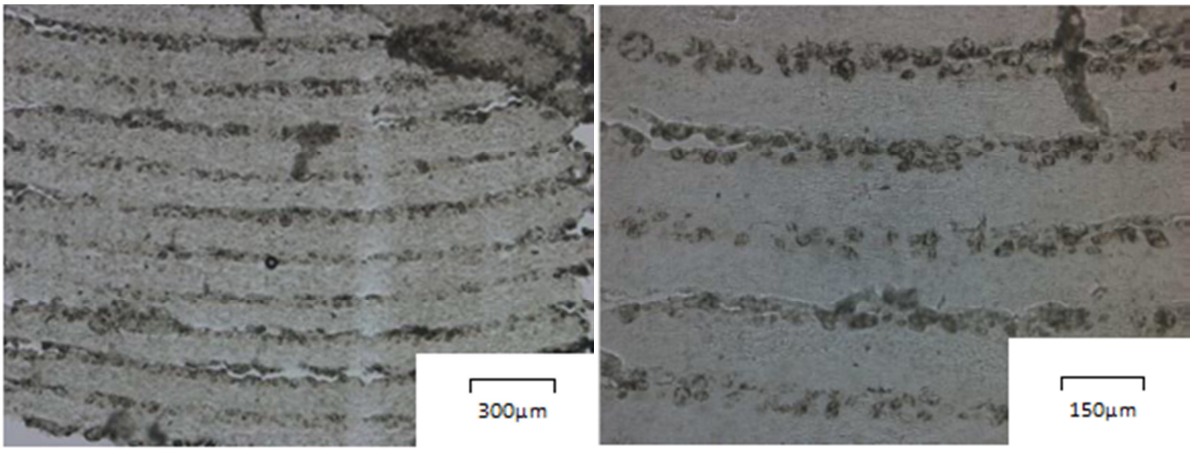

Figure 11: University of Louisville Laser Sintering Microtoming Sample (Gornet 2010)

Based on the various research and characterization that has been done previously and discussed in this section, there are several key takeaways that will impact this research:

- Intrinsic raw material properties have an effect on processing in laser sintering.
- The Degree of Particle melt study and the microtoming specimens appear to indicate a morphology that justifies weak layer-to-layer adhesion.
- Correlation of energy density to mechanical properties shows a strong correlation of energy density to tensile strength but with significant variability with respect to elongation at break.

1.6: FRACTURE MECHANICS

Based on the previous research done on the failure mechanisms in laser sintered polyamide (Starr, et al. 2008), the yield stress and ultimate tensile strength are relatively consistent among reported results and are comparable to reported material properties in other processes. The key deficiency in the laser sintering process is an elongation at break that is significantly lower than other manufacturing processes. If there is no significant degradation in the intrinsic material properties, this fast fracture of tensile specimens contributes to a decreased elongation. Fracture mechanics is the study of ductile materials failing due to brittle failure. There are three modes of failure with the primary failure mode in tension being Mode I, seen in Figure 12.

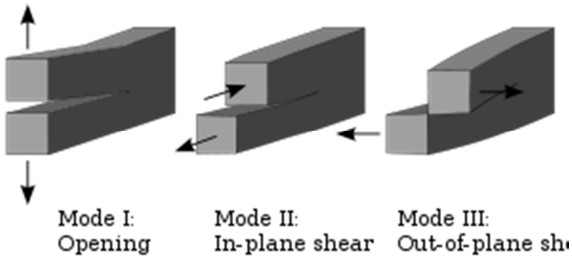

Figure 12: Fracture Mechanics Failure Modes taken from (Twisp 2008).

The critical yield stress, or fracture stress (σ_f), of polyamide is significantly greater than what is observed in laser sintering while the fracture toughness remains the same. The correlation of fracture toughness to critical yield stress is shown in Equation 2. This correlation assumes that there is a crack within a part (a) or specimen and that the geometry of the crack and specimen can be quantified which produces a shape factor (Y). A sampling of shape factors is shown in Figure 13.

$$\mathbf{K_{Ic} = Y\sigma_f\sqrt{\pi a}} \qquad \textbf{(Equation 2)}$$

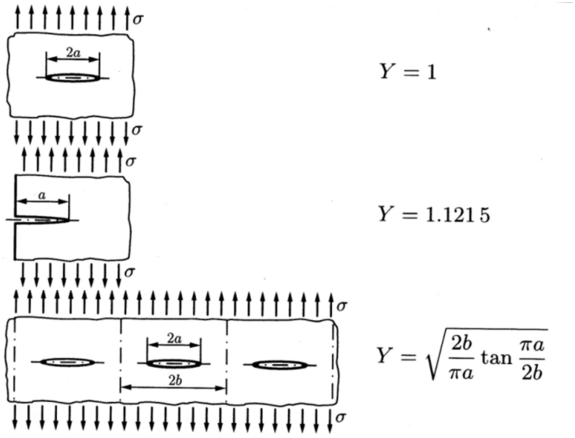

Figure 13: Fracture Mechanic Shape Factors (Roesler, Harders and Baeker n.d.)

1.7: PROBLEM STATEMENT

This work will investigate the primary contributors to the mechanical failure of laser sintered nylon polyamide specimens. It is theorized that poor layer-to-layer adhesion, a primary

culprit in additive manufacturing anisotropy, can be attributed to intralayer porosity. The relative porosity of the interfacial boundary layers contributes to decreased ductility and fracture stress.

EXPERIMENTAL PROCEDURE

2.1: PRODUCTION OF LASER SINTERING SPECIMENS

All specimens in this study were built on machines owned and operated by Harvest Technologies in Belton, TX. The specific machines used were 3D Systems™ sPro 60® or equivalent seen in Figure 14. These machines are the same as the base Sinterstation® 2500 with a 70 W CO_2 laser, the addition of digital scanning, and active thermal control through the use of a black-body reference heat source. Samples were made in both PA 12 (Duraform® PA) and PA 11 (Duraform® EX and ALM FR-106).

Figure 14: 3D Systems™ sPro 60® Laser Sintering Machine

A total of 24 PA-12 specimens were produced and evaluated. These specimens were segregated based on the tensile results as described in Section 2.5, with selected samples being evaluated using SEM. After tensile testing, specimens were sputtered with gold particles for increased resolution and evaluated using SEM. Eight of the 24 specimens were used with redundant specimen data being discarded. Figure 15 shows an array of 8 tensile specimens with 4 being oriented primarily in the z-axis, and 4 being oriented primarily in the x-axis. Three total builds were used with varying laser powers from 10% to 100% of optimized parameters to illustrate the full range of failure mechanisms typically seen.

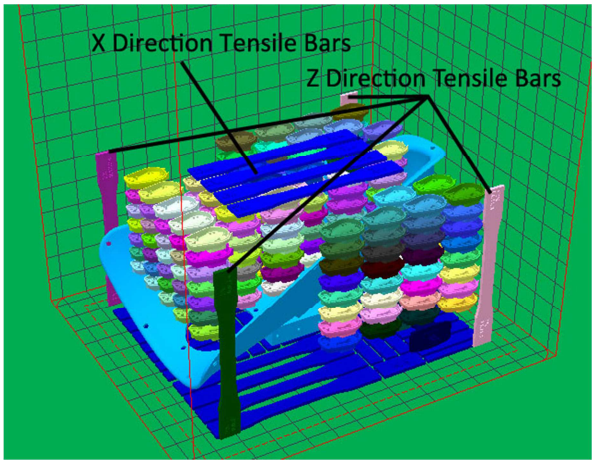

Figure 15: Tensile Specimen Location in Build

2.2: MODELING INTERFACE BOUNDARY LAYER TENSION SPECIMEN

The custom tension specimen used for characterizing the interface boundary layer was created in STL on an IBM PC with Magics 15 Rapid Prototyping Software from Materialise. The native ASTM D638 specimen was scaled and sectioned to insert a closed pack array of hemispheres to simulate a layer of powder, seen in Figure 16. The spheres were modeled at 0.100" diameter with the cross-section at the interface measuring 0.300"x0.500". The half of the tensile bar that had a flat surface was combined with the specimen having the hemispheres to create a single tensile specimen STL file, seen in Figure 17. This operation was repeated for h/r Ratios of 0 to 1 at 10% increments, with h representing the depth of penetration of an intersecting plane with r, which represents the hemisphere's radius. With the hemispheres measuring 0.050" radius, the interface was moved 0.005" for each subsequent sample. The h/r ratio dimensions are detailed in Table 3. Specimens were labeled with the software to qualify the resultant h/r ratio of each.

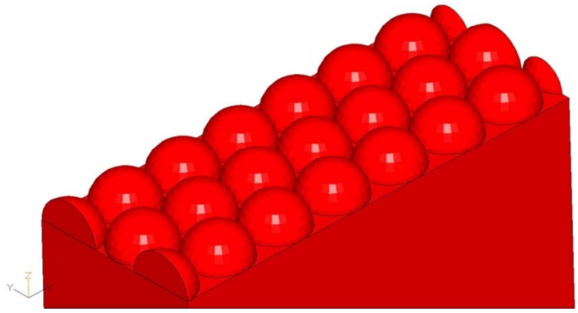

Figure 16: Model of Close Packed Hemispheres on Tension Specimen

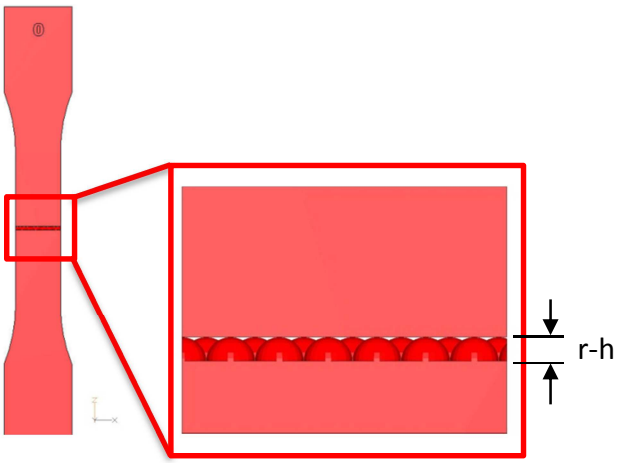

Figure 17: ASTM D638 Tension Specimen with Visible Interface Boundary

2.3: PRODUCTION OF INTERFACE BOUNDARY LAYER SPECIMENS

Interface boundary specimens were produced in optimized production builds and oriented primarily in the x-axis. Orientation of these specimens in the x-axis eliminates the possibility that layer-to-layer adhesion will impact test results. These tensile results were used to quantify the geometry effect of the interface boundary layer. Specimens were built in the same orientation as the x-axis specimens shown in Figure 15 using PA-11 (ALM FR-106) so that the testing could capitalize on the contrast afforded by a material that typically achieves greater than 50% elongation in the x-y plane.

2.4: TENSION TESTING

Tensile properties were measured using an MTS Insight 10 at Harvest Technologies, shown in Figure 19. The specimens produced were ASTM D638 specimens with a cross-sectional area at fracture of roughly 0.125" X 0.500". The procedure for pulling the specimens was to use a 0.20 inch/minute rate with an extensometer that conforms to ASTM E83 class B2 with a range of at least 50%. The extensometer is limited to 50%; thus, no quantifiable measurements exceeding that limit are recorded.

2.5: SCANNING ELECTRON MICROSCOPY (SEM)

The fracture surfaces were evaluated using a JEOL JSM 5610 Scanning Electron Microscope (SEM) at The University of Texas at Austin with a tungsten filament, 3 nm resolution, and magnification up to 300,000.

Figure 18: MTS Insight 10, Extensometer, and Specimen

2.6: CORRELATION OF PHYSICAL AND VISUAL PROPERTIES

The objective of this part of the research was to correlate the mechanical properties observed with visual inspection to obtain a better understanding of the failure mechanisms of laser sintered parts. The material was 3D Systems™ Duraform® PA, a Nylon 12 polyamide. Tension specimens were added to a production build to evaluate the surface of a tension specimen and the fracture surfaces of both X and Z direction tension specimens. The process settings and build location of test specimens were such that three failure modes typical for laser sintering would be present for this experiment:

1. Delamination – A special type of brittle fracture that is characterized by very weak layer-to-layer adhesion. The fracture of a z-axis oriented specimen will break exclusively in the region between layers. Delaminated Z-direction specimens were processed at standard thermal parameters with laser power at less than 50% of recommended parameters.

2. Brittle Fracture – Failure of a laser sintered specimen in tension within the elastic deformation range of a standard stress-strain curve. Fracture stress is less than yield stress with strains less than 10%. Typical fracture surfaces have a 45^{o} shear fracture.
3. Ductile Fracture – This is the desired failure mode. A ductile fracture will yield nearly isotropic parameters. Processing parameters have been optimized for build quality with a sacrifice in efficiency and cost. There are two characterized ductile failure modes:
   a. Fracture Limited Ductility -- A fracture that occurs after the onset of strain hardening and typically before UTS and the onset of significant necking. Strains are typically 15-25%.
   b. Full Plasticity Failure – Fracture occurring after the onset of necking at UTS. If this level of strain is reached, it is very common that failure will not occur until 40-60% strain.

2.7: Evaluation of Melt Flow Rate on Specimen Failure Using Injection Molding

It has been observed that a primary contributor to poor mechanical properties of laser sintered components is the thermal aging, or degradation, of the material. Continuous exposure of the unsintered material to the elevated thermal environment causes cross-linking in the polymer chain and contributes to decreased physical and mechanical properties. As the material undergoes thermal aging, the viscosity of the material is seen to increase and can be evaluated using a melt-flow measurement tool.

A key consideration in evaluating specimen failure is whether this material degradation is an intrinsic material defect or whether this change in viscosity has an effect on process specific layer-to-layer adhesion. Unusable polyamide powder was segregated from production at Harvest Technologies and its viscosity (melt flow rate) evaluated. This used polyamide powder was then processed in a BOY laboratory injection molding machine at The University of Texas to produce several tension coupons.

2.8: Melt Flow and Injection Molding Device

Previously used powder was measured in Dynisco Melt Flow Indexer at Harvest Technologies and then used as feedstock to run standard ASTM D638 tension specimens at The University of Texas. The melt flow indexer was used in conjunction with a drying oven, a calibrated balance scale, and Dynisco's Polymer Test MIWORKS melt index test database in order to quantify the Melt Flow Index (MFI) of previously used powder compared to unused (virgin) powder. This device is designed to meet all of ASTM D1238 melt conditions. The BOY Laboratory injection molding machine was used to process the feedstock with standard PA settings using an ASTM D638 mold. Resultant tension bars were then tested at Harvest Technologies in the device described in section 2.4.

2.9: Compression and Injection Molding Comparison

An outside laboratory (Polyhedron Laboratories) was commission to make ASTM D638 tensile coupons in both compression molding and injection molding. A G-100T Model Morgan Press was used to create the injection molding specimens and processed at 450F with 40 hr conditioning. A PHI 50 ton press was used to create the compression molding specimens at 430F and 40 hr conditioning. The laboratory used an Instron Model 1114 tensile tester with an Electronic Instruments Research laser extensometer.

2.10: Geometric Consideration of the Interface Boundary Layer

When laser sintered specimens are observed optically, there is a visible boundary layer between subsequently fused layers. This boundary layer is exclusively seen with X-Y plane orientation. This interface boundary layer appears to be a primary culprit in decreased mechanical properties and can be characterized as a layer of coplanar voids. Therefore, tensile specimens were created using CAD to simulate this boundary layer with varying degrees of severity. These specimens were then processed in the stronger X-direction to isolate the effect of the decreased z-direction mechanical properties on this experiment.

Figure 17 illustrates the CAD model that was created to simulate coplanar powder particles. The tension bar was scaled up from a standard ASTM D638 tension bar. The particle diameter was modeled at 0.100".

The two halves of the tensile bar were created independently to allow for a variation in the interface interference between a plane on one half and coplanar spheres on the other. This interface was defined by an h/r ratio seen in Figure 20. An h/r ratio (described in Section 2.2) of 0 had the spheres just touching the plane as illustrated in Figure 17. A ratio of 1 will have no effective interface boundary and is equivalent to a solid tensile bar. Eleven tensile specimens were produced with an h/r Ratio from 0 to 1 at an increment of 0.1. The material used was a polyamide 11 in an optimized production build. Optimized polyamide 11 production builds typically yield the highest mechanical properties and should provide the greatest contrast for the varying h/r ratio specimens. This coplanar void creation is analogous to a "paper-towel" perforation with varying degrees of perforation or void density.

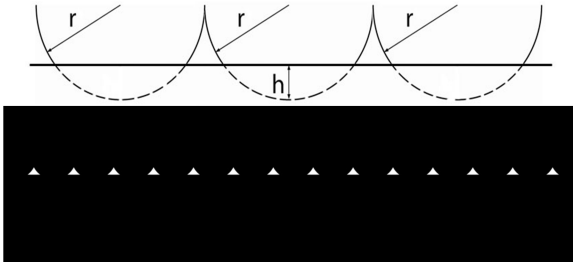

Figure 19: Schematic of h/r ratio

RESULTS

3.1: TENSION SPECIMEN CHARACTERIZATION

The tension testing performed yielded the results shown in Table 1. Data from 8 specimens are listed in this table and illustrated in the SEM photographs. Tension specimen nomenclature identifies the geometric location of the sample in the build as well as the build orientation. A "zx" specimen would be oriented primarily in the z-axis with the secondary axis oriented in the x-axis, consistent with ASTM F2921. An "x" or "y" specimen would be oriented flat in the x-y plane with the primary length along the x or y-axis, respectively. The x and y-axis specimens yielded better mechanical properties and more consistent results. The three primary failure mechanisms discussed in section 2.8 and enumerated in Table 1 can be seen in Fig. 21.

Table 1: Tensile Properties and Fracture Mode of PA-12

Sample	Energy Density J/mm^3	Ultimate Tensile Strength (UTS) psi	Elongation at Break (EOB) %	Fracture Mode
ZX 12.0.3	0.1	494	1	Delamination
ZX 0.0.3	0.1	2969	1	Delamination
ZX 0.12.3	0.1	1278	1	Delamination
ZX 13.11.3	0.2	5164	3	Brittle
X 4.2.8	0.2	5886	7	Brittle
X 4.3.8	0.2	5991	6	Brittle
X 4.4.8	0.2	5763	7	Brittle
+Y 1.4.1	0.3	6099	44	Ductile

[1] Ductile fracture taken from independently optimized build.

Delamination Brittle Fracture Ductile Fracture

Figure 20: Photographs of Tensile Specimen Failure Mechanisms. Specimens pictured are 1.50 inches in width. The right specimen is 0.50 inches thick with the left two being 0.25 inches thick.

3.2: MORPHOLOGY OF PA-12 TENSILE SPECIMEN FRACTURE SURFACES

The SEM image shown in Figure 22 shows an x-y sample with layering in the z-axis shown vertically. When inspected, the photographs show clear patterns for the layers with elongated horizontal voids between layers. Approximately energy density is approximately 0.10 J/mm^3 with an energy-to-melt ratio of 1.0. Figure 23 is a magnified region of the same sample. It illustrates a single layer with voids both above and below the fully melted layer. There are also fully dense regions where there was sufficient energy to melt the layers together, creating a more homogeneous region.

The surface of a Duraform PA (PA-12) XY tension specimen is illustrated in Figures 24 and 25. This shows the upper facing surface and the surface to which the loose powder must be bonded by the laser. The average particle size is roughly 50 microns and individual particles can be seen to be melted in Figure 25, appearing like a lily pad or pancake structure. Some particles can be seen to have melted with other particles while others appear to be isolated with voids between particles. Of particular interest in Figure 25 is the 250μm boulder looking particle in the center of the micrograph.

The fracture surfaces of Duraform PA (PA-12) Z tensile specimens are shown in Figures 26 through 31. These specimens were evaluated with the camera parallel to the z-axis looking at

a fracture generally in the x-y plane. Delamination is illustrated in Figures 26 and 27, brittle fracture in Figures 28 and 29, and ductile fracture in Figures 30 and 31. The surfaces photographed in Figures 26, 27, 30, and 31 were consistently parallel to the x-y plane. The fracture surfaces photographed in Figures 28 and 29 were evaluating a 45° shear surface.

3.2.1: Morphological Observations

When evaluating the image of the fracture surface shown in Figure 22, a periodicity can be observed. With the understanding that the z-axis is the primary direction for added layers, a pattern of voids between layers is apparent. This stratification contributes to anisotropic material properties and significant weakness if a tensile stress is exerted parallel to the z-axis. In addition, these patterns of voids contribute to a significant reduction in elongation and ultimate tensile strength.

When looking at the upper facing surface of the specimen shown in Figure 25, it appears that the 250μm particle was formed when several particles melted together but did not fully adhere to the surface. When the particles cooled, there became a condensed grouping of several melted particles with a surrounding void. This voided region may contribute to voids in the part unless sufficient energy is used to re-melt these particles and bond with the surrounding surface.

It is apparent from the analysis of these samples that the cracks propagate through voids created by a lack of full melt between layers. The general observations for each fracture mode are listed below:

- Delamination fracture surfaces can be seen in Figures 26 and 27. These images show a fracture of the Z specimen that is parallel to the x-y plane. Three distinct layers are represented as the crack propagation followed the area between two parallel layers and then migrated to neighboring layers. This pattern, when examined in Figure 27 shows that the particles are roughly 50 microns in diameter, which corresponds to the average particle size of the raw material. When compared to the morphology of the top layer (Figures 24 and 25), it can be seen that the bottom layer has very little bonding to the previous layer.
- Brittle fracture surfaces can be seen in Figures 28 and 29. Voids are isolated and somewhat periodic, with similar size and spacing. Fracture surfaces show a ductile tear with transgranular fractures or river marks. These fracture surfaces are similar to the ductile specimen (Figure 30) but with void fraction on the failure surface higher.
- Ductile fracture surfaces can be seen in Figures 30 and 31. With an elongation of 44%, it may be observed that there is void nucleation where the material tore apart from itself. From Figure 31 shards of material and a very dense surface are observed.

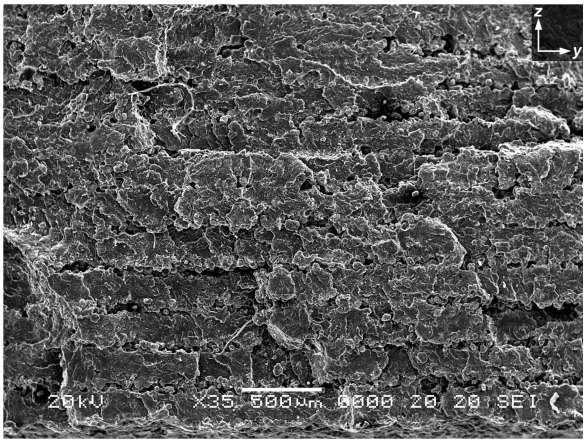

Figure 21: SEM of X Tensile Bar Fracture Surface. (35x) PA-12, 0.1 J/mm^3

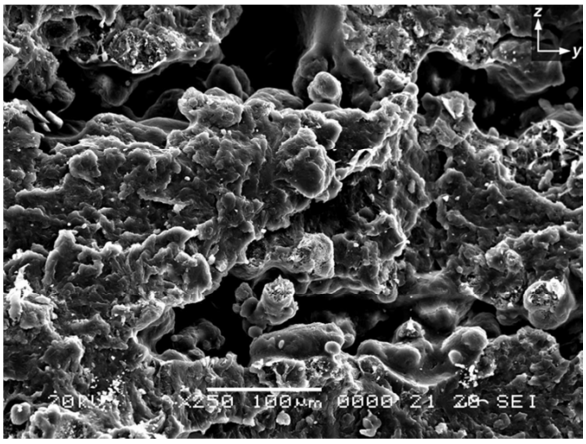

Figure 22: SEM of X Tensile Bar Fracture Surface. (250x) PA-12, 0.1 J/mm^3

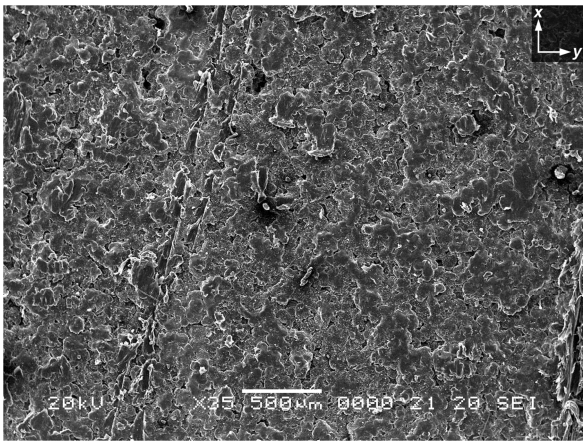

Figure 23: SEM of X Tensile Bar Top-Facing Surface. (35x) PA-12, 0.2 J/mm^3

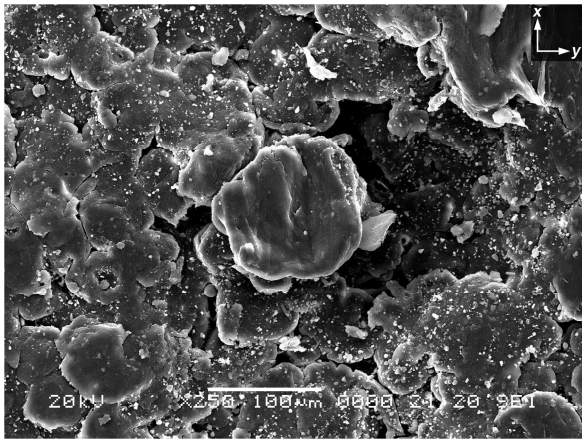

Figure 24: SEM of X Tensile Bar Top-Facing Surface. (250x) PA-12, 0.2 J/mm^3

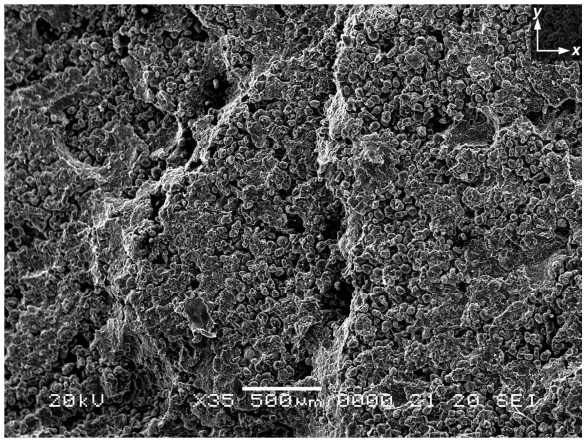

Figure 25: SEM of Z Tensile Bar – Delamination. (35x) PA-12, 0.1 J/mm^3

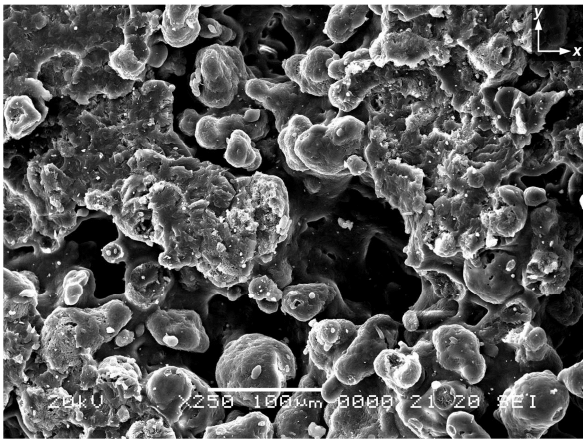

Figure 26: SEM of Z Tensile Bar – Delamination. (250x) PA-12, 0.1 J/mm^3

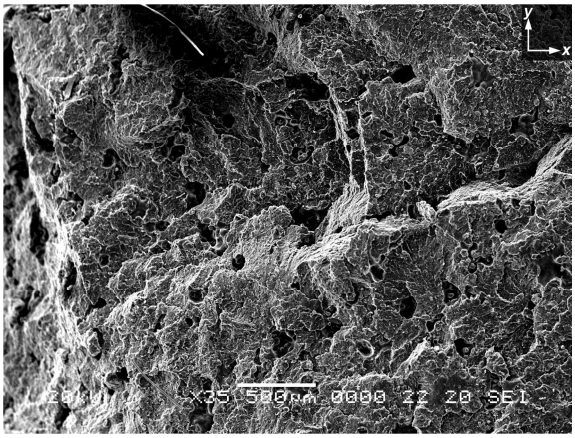

Figure 27: SEM of Z Tensile Bar – Brittle Fracture. (35x) PA-12, 0.2 J/mm^3

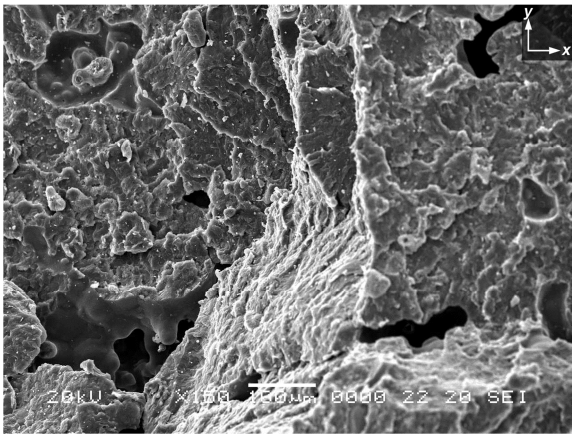

Figure 28: SEM of Z Tensile Bar - Brittle Fracture. (250x) PA-12, 0.2 J/mm^3

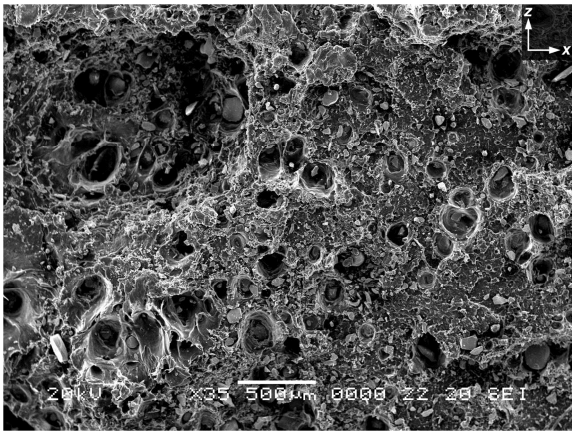

Figure 29: SEM of Y Tensile Bar - Ductile Fracture. (35x) PA-11, 0.3 J/mm^3

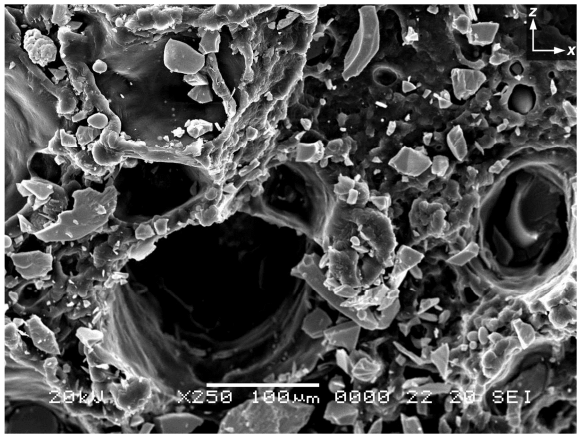

Figure 30: SEM of Y Tensile Bar - Ductile Fracture. (250x) PA-11, 0.3 J/mm^3

3.3: INJECTION MOLDED TENSION SPECIMENS

Standard injection molding parameters from a materials handbook were used to create fully dense ASTM D638 tensile specimens in-house in the Engineering Teaching Laboratory facility at The University of Texas at Austin. (ASM Engineering Materials Handbook n.d.) This particular machine was not in the greatest state of repair, but was sufficient for creating several tensile specimens from used PA-12 material. The powder was poured directly into the feed hopper of the injection molder and processed manually. The results of the tensile tests are presented in Table 2. Both specimens exceeded the range of the extensometer (50%) with one specimen pulled until it reached the mechanical limits of the load cell.

Table 2: Injection Molded Tensile Results of Previously Used PA-12

Sample	σ_y (psi)	UTS (psi)	EOB %	Fracture Mode
1	3884	5572 psi	>50%	Ductile
2	3937	5530 psi	>200%	Ductile

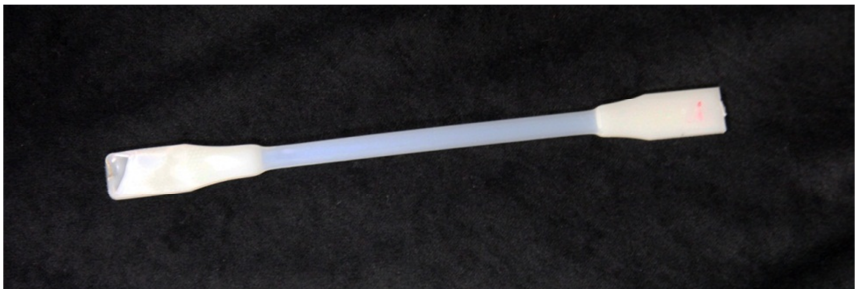

Figure 31: Photograph of Injection Molded Specimen

3.4 External Injection and Compression Molding Specimens

Polyhedron Laboratories, Inc. of Houston, TX provides plastics, polymers, and rubber testing. Laser sintering grade raw Nylon-11 material was provided to them for testing. The results reported can be seen in Table 3 below.

3.5: h/r Ratio Tension Specimens

Two builds of 11 samples each were built and evaluated, with one set of samples having a finished surface and the other set having no post finishing done. There was no difference in ultimate tensile strength and elongation between builds. The data presented in Table 3 and Figure 32 are from the unfinished tensile specimens. There is a definite grouping of parameters for h/r ratios of 0.6 to 0.9 that corresponds with the strain hardening during necking of the specimens.

It can be seen that all h/r ratio specimens followed the same stress-strain curve seen in Figure 33. The data collected was graphed in Figure 34 to illustrate the patterns observed in three primary regions of fracture. Note that delamination is a special case of brittle fracture.

Table 3: Injection and Compression Molded Tensile Results of PA-11

Analytical Report

		Tensile Properties by ASTM D 638					Izod Impact by ASTM D256	
Sample		Tensile Strength (psi) at Yield	Tensile Strength (psi) at Break	% Elongation at Yield	% Elongation at Break	Tangent Modulus (psi)	Impact (ft·lbf/in)	Failure Type
Injection Molded Nylon 11		5812.8	4891.5	23.9	128.0	107,316.8	1.913	C
		5985.2	5026.0	20.4	172.6	125,160.8	1.651	C
		6067.8	7015.0	19.5	278.7	136,864.1	1.788	C
		5879.1	5587.6	25.5	320.0	136,686.8	1.742	C
		5844.1	5302.7	23.9	309.3	142,370.2	1.651	C
	AV =	5917.8	5564.6	22.6	241.7	129,679.7	1.749	
		± 106.1	± 853.8	± 2.6	± 86.3	± 13,984.7	± 0.109	
Compression Molded Nylon 11		7186.6	7014.0	22.2	23.5	172,307.4	1.356	C
		7137.8	6983.5	27.4	33.0	208,671.6	1.281	C
		7274.9	6937.7	26.9	30.1	204,679.0	1.271	C
		7325.1	6956.8	27.3	33.3	168,026.9	1.271	C
		7350.3	5559.0	21.8	72.5	175,087.0	1.228	C
	AV =	7254.9	6690.2	25.1	38.5	185,754.4	1.282	
		± 90.6	± 633.0	± 2.9	± 19.4	± 19,314.6	± 0.047	

Failure Type: C = Complete

Table 4: h/r Ratio Tensile Results of XY Oriented PA-11

Sample	h/r Ratio	σ_y (psi)	UTS (psi)	EOB %
1	0	2772	2954	4
2	0.1	2854	3124	4
3	0.2	3028	4021	6
4	0.3	3056	4976	7
5	0.4	3163	5312	9
6	0.5	3047	5468	9
7	0.6	2824	5882	17
8	0.7	3090	6130	17
9	0.8	3225	5994	16
10	0.9	3214	6133	18
11	1.0	3015	7391	>50*

* Specimen exceeded extensometer limit of 50%.

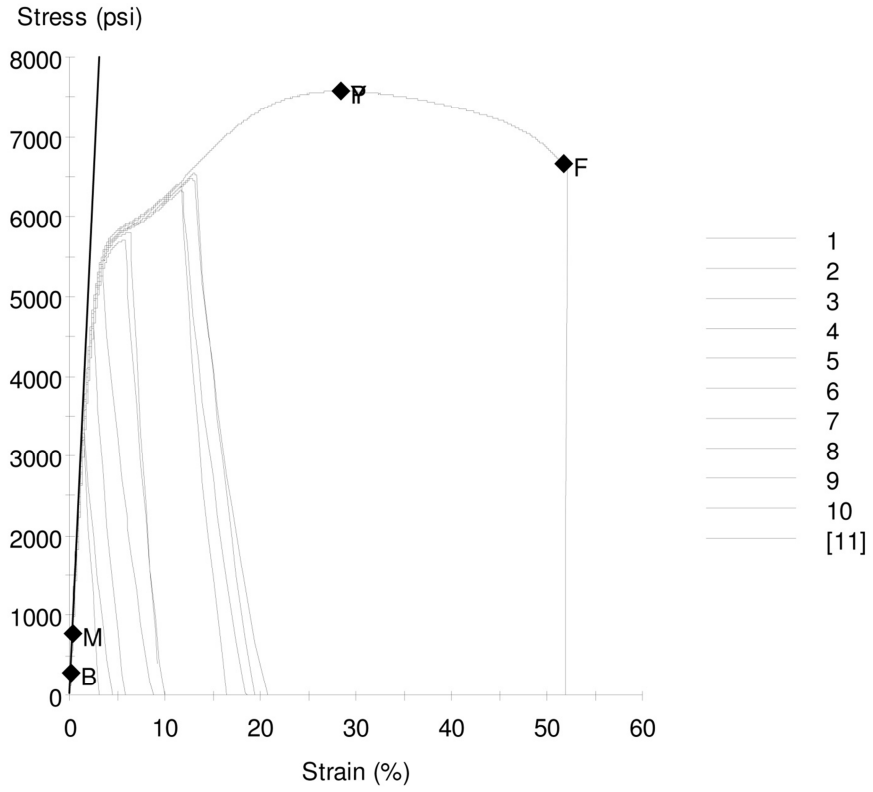

Figure 32: Stress-Strain curve for h/r Ration Specimens

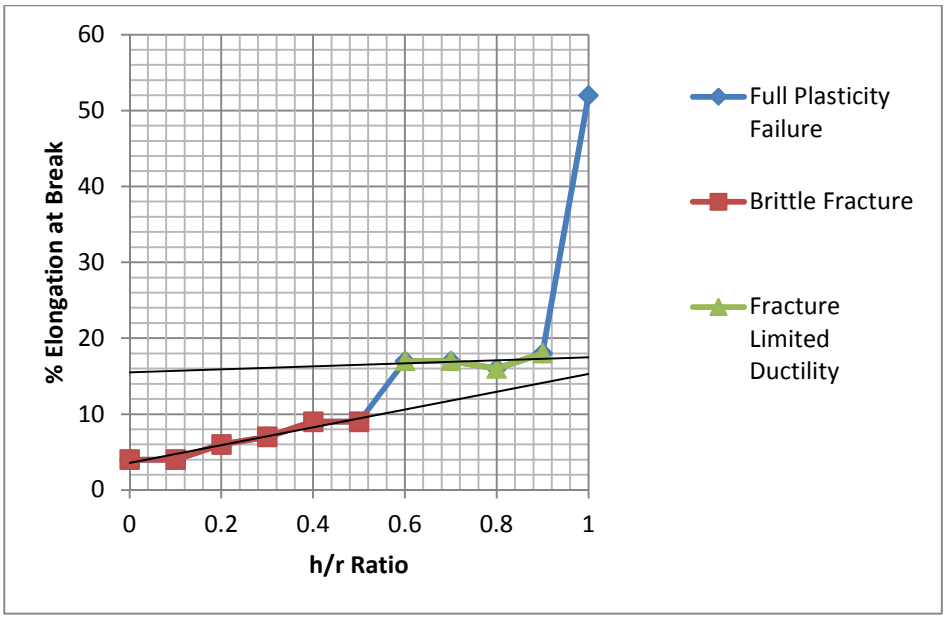

Figure 33: Trends in h/r ratio tension properties

3.5: X-RAY DIFFRACTION

Another mode of decreased mechanical properties is seen in specimens that are near the build extent boundaries. Parts and specimens that are near the boundaries undergo a higher rate of cooling. It has been observed in production builds at Harvest Technologies that the placement of specimens up to 0.5" deeper in a build yields better mechanical properties. Table 4 illustrates this with a clear increase in elongation with an increased depth that corresponds with a slower cooling rate.

Table 5: Effect of Recrystalization on Tensile Properties of XY Oriented PA-11

Specimen	Depth (in)	σ_y (psi)	UTS (psi)	EOB %
1	-.125	2906	4757	11
2	-.461	2933	4749	12
3	-.797	2872	4876	14
4	-1.133	2891	5007	15

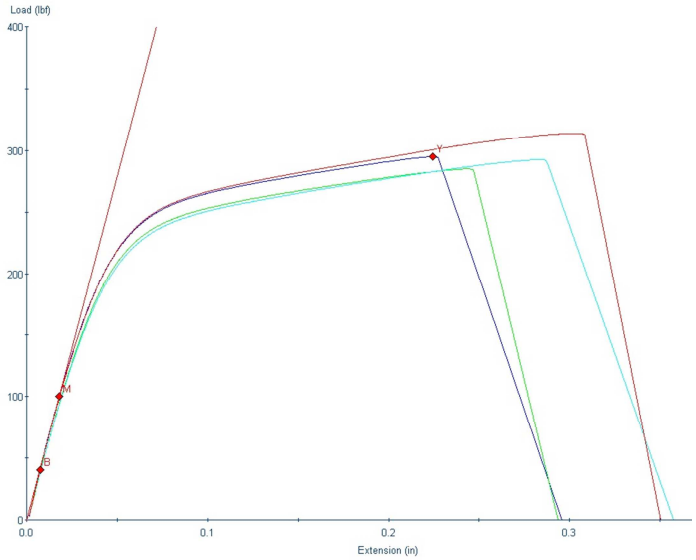

Figure 34: Stress-Strain curve for x-ray diffraction specimens

It was theorized that the rate of cooling could correspond to a degree of crystallinity in the resultant specimens. Figure 36 shows x-ray diffraction results for four specimens listed in Table 5 and Figure 35. The periodicity in the x-ray diffraction figure is a function of the base material and the width of the peaks and valleys represent the level of crystallinity of the material. When observing these plots, periodicity and slopes appear equivalent. Based on these results, there appears to be no functional difference in crystallinity that could contribute to an increase or decrease in mechanical properties. Therefore, it is more likely that there is an optimal thermal processing dwell time above the recrystallization point promoting a stronger inter-layer adhesion.

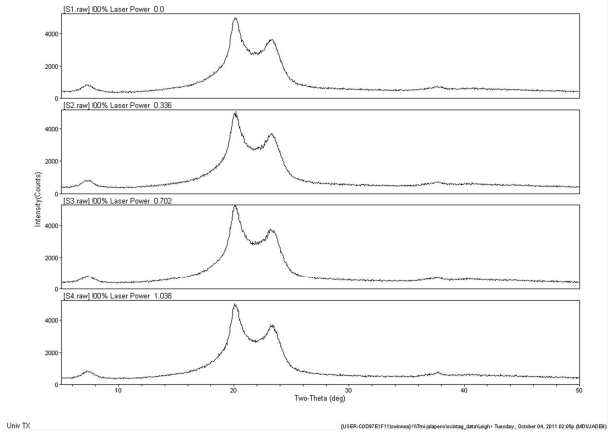

Figure 35: X-ray diffraction results showing equivalent periodicity and crystallinity.

DISCUSSION

4.1: MORPHOLOGY OF PA-12 TENSILE SPECIMEN FRACTURE SURFACES

It is apparent that the material properties observed in Table 1 can be correlated to the extent of voids present between sintered layers. With very little adhesion between layers,

delamination and elongation values near 1% are seen. With sufficient energy to melt through the target layer into the previous layer, a fully dense part will yield elongations well above 10%. As the layer has a higher degree of melt, the voids will decrease through the brittle range until the voids no longer contribute to the fracture.

Figures 22 and 23 are photographs of specimen voids being created between subsequently built layers through the lack of complete particle melt to the previous layer. Figure 37 shows a larger separation between layers and represents the sample seen in Figures 26 and 27 (delamination). Since the voids are coplanar, they are analogous to pre-existing cracks. The crack propagation in this example will cause a shear between layers resulting in delamination.

Figure 38 represents the sample seen in Figures 28 and 29 (brittle fracture) with voids present, but with the voids being isolated and periodic. The crack propagation in this example is much less directional since the voids are no longer exclusively coplanar. A fracture may originate between specific layers, but will typically travel through voids in neighboring layers since the distribution of voids is much less ordered.

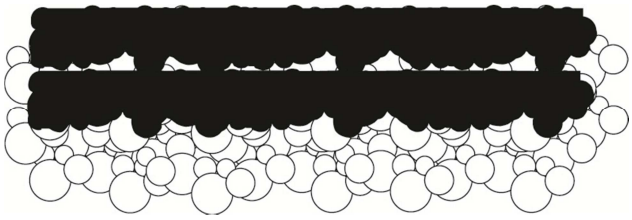

Figure 36: Lightly adhered layers contributing to delamination.

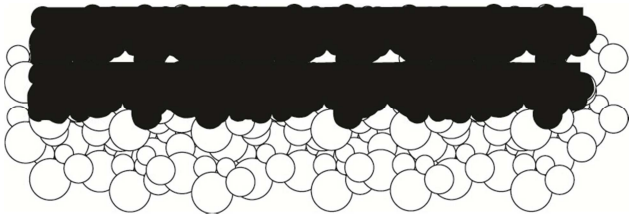

Figure 37: Incomplete fusion contributing to brittle fracture.

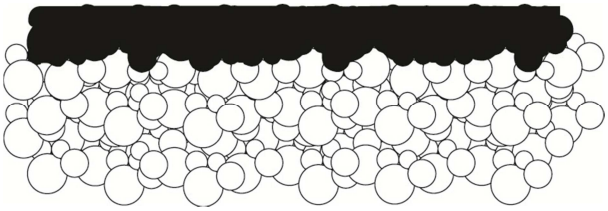

Figure 38: Initial Layer of Sintered Powder

Figure 39 is a graphical representation of an initial layer created in the laser sintering process. The depth of this layer is dependent upon the laser energy, but regardless of the amount of energy on the first layer, the downward facing surface will be defined by the raw material particle size as seen in Figure 26. The top of the layer is flat and will look like the surfaces seen in Figure 24 and 25. This irregular downward facing surface is the impetus for void creation.

To insure the best properties of a part created though the laser sintering process, layers must be processed in such a way as to minimize or eliminate voids between layers. Voided regions between layers define the fracture mode. The h/r ratio experiment discussed in section 2.11 is illustrated again in Figure 40. The interface boundary layer created with the h/r ratio

shown in Figure 39 illustrates the close proximity to the coplanar voids illustrated in Figures 37 and 38.

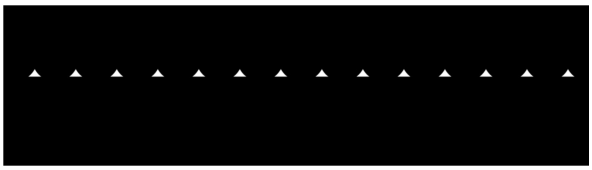

Figure 39: Simulated interface boundary ratio using an h/r ratio

4.2: Effect of Reused Powder on Particle Melt in Injection Molding and Comparison of Laser Sintering to Compression Molding

Based on the tensile data acquired, it was apparent that degraded powder did not yield poor mechanical properties when injection molded. This test provides us a good degree of confidence that the degradation of mechanical properties in the laser sintering process is not an intrinsic material property defect but a property that affects the processing of the polyamide material in laser sintering. The melt flow index (MFI) of new powder is generally a value of 30g/10sec which corresponds to a low viscosity and relatively high melt flow rate. An MFI of 1g/10sec is a very low flow rate with a high viscosity. The material used in the injection molding tension specimens was previously used with an MFI of 1g/10sec.

When comparing the mechanical properties measured in laser sintering, it is apparent that laser sintering is comparable to compression molding while exhibiting limited ductility when compared to injection molding. The fact that compression molding and laser sintering do not have the benefit of shear and complete mixing contributes to weaker specimens due to polymer melt surfaces that are not sufficiently healed. There can also be a presence of voids in these melts that is not typically seen in injection molding which can contribute to fast fracture.

4.3: Coplanar Void (h/r Ratio) Behavior

The existence of an interface boundary layer can be illustrated in Figures 22 and 23 from the SEM images. In addition, work done at the University of Louisville with microtoming and optical microscopy of samples shows evidence of a boundary region between layers. The work cited here and in Figure 11 is not published at the time of this writing. (Gornet 2010)

The images obtained from the University of Louisville show a cross section in a sample that is oriented the same as the fractures shown in Figure 22. The samples were created by using a microtoming technique common in medical pathology. The samples were sliced in layers roughly 5 microns thick to evaluate individual layers. It can be seen in Figure 11 that the fused layers (lighter color) are fully dense and the particles at the bottom of the layer (darker) are nylon particles that were not sintered. It can also be observed that there are several tears in the sample shown in Figure 11 that correspond with these darker (unmelted) regions.

When analyzing the graph in Figure 34, there are two distinct trends present with an outlier at an h/r ratio of 1.0. An h/r ratio of 0 to 0.5 represents fracture during elastic strain and before strain hardening. There is also a grouping of these regions observed in the stress-strain curve in Figure 33.

The use of an h/r ratio helps quantify the failure modes in a macro scale and can help in identifying material process improvements that may help on a micro scale. This correlation is significant.

4.3: PART DENSITY OR CRITICAL CRACK SIZE

One metric that is commonly used to evaluate laser sintering parts is the density of the specimen. The boundary layer density was calculated using a slice taken from the CAD file of the periodic layer and interface boundary (r-h). The CAD file volumetric density data is plotted with the corresponding h/r ratio in Figure 41. This figure shows the density of a single layer based on the corresponding h/r ratio. If layers are consistent throughout the build, the resultant part density would be the same as an individual layer. The issue with this assumption is that the mechanical properties do not show the same trend when comparing the elongation data in Figure 34.

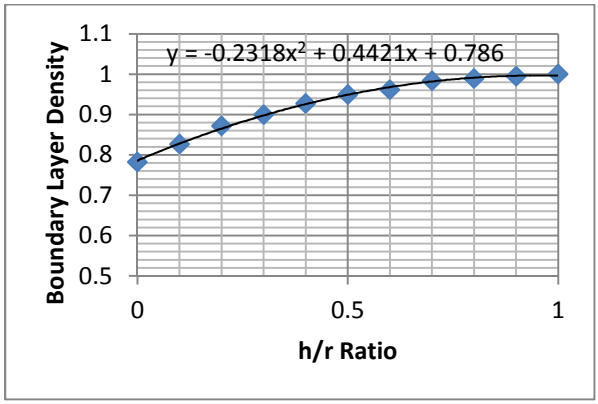

Figure 40: Correlation of effective part density and h/r ratio.

It is possible that the jump in elongation data shown in Figure 34 when going from an h/r ratio of 0.9 to 1.0 is that the effective crack size hits a critical value. The critical crack size can be calculated using the formula shown in Equation 2 and reduced to Equation 3. To calculate the smallest critical crack size (a_c), it is assumed that there is a simi-infinite plate and a single crack, using a value of 1 as a shape factor (Y). The critical crack size is assumed to be critical at the point the plate would yield vs. fail due to fast fracture. Therefore, the yield stress would be used as the fracture stress. The data and results for the critical crack size calculations for injection molded polyamide are shown in Table 6.

$$a_c = \frac{1}{\pi}\left(\frac{K_{Ic}}{Y\sigma_f}\right)^2 \qquad \textbf{(Equation 3)}$$

Table 6: Theoretic Critical Crack Size of PA-11 and PA-12 (CES Edupack n.d.)

Material	σ_y (psi)	K_{Ic} (psi$\sqrt{in}$)	Y	a_c (in) - min
PA-11	8300-8700	3330-7310	1	0.051
PA-12	3000-6110	1840-5530	1	0.1197

When evaluating the relative porosity of the interface boundary layer and disregarding the porosity as a whole, more intuitive results are obtained. The failure of any specimen in additive manufacturing will happen at that one layer or layers that are the most porous locally (largest a_c). Given that fact, the relative porosity of the boundary layer in the h/r ratio

experiment was calculated and the results were plotted in Figure 42. The general form of the equation given by Haynes is shown in Equation 4 where ε is the relative porosity and C is a constant. (Haynes 1977)

$$\text{Relative Elongation} = \frac{(1-\varepsilon)^{1/3}}{(1-C\varepsilon^2)^{1/2}} \qquad \text{(Equation 4)}$$

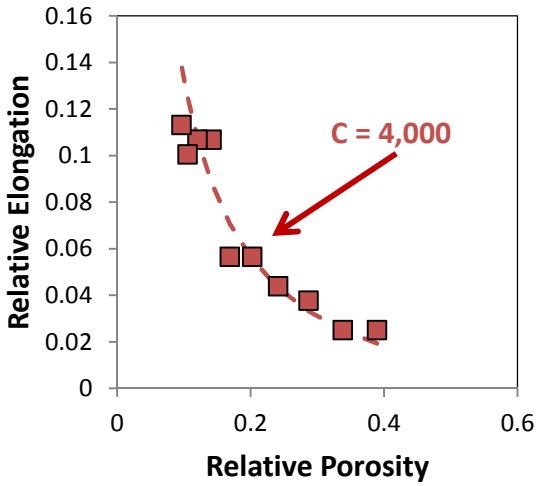

Figure 41: Relative porosity of interface boundary layer vs. relative elongation.

When correlating fracture stress to the morphology observed, it is apparent that there is sufficient intralayer porosity for one or more critical cracks exist in the specimen prior to loading in the "delamination" examples shown in Figures 33 and 34. As the specimen undergoes a tensile load and starts to elongate, fast fracture occurs due to a pre-existing crack equal to or greater than the critical crack size (a_c), governed by Equation 3.

The intrinsic cracks in samples that fail after the onset of strain hardening (again seen in Figures 33 and 34) are less than a_c but are of sufficient density to inhibit the onset of significant necking. For those specimens that fail at strains seen after the onset of necking at UTS the relative porosity is greatly reduced. It is very rare to see z-axis strains approach 50% as shown in Figure 34 for the h/r ratio of 1 due to the intralayer porosity.

CONCLUSIONS

Laser sintered specimens are comparable to compression molding specimens in modulus, ultimate tensile strength, and elongation at break. Laser sintering exhibits a significantly reduced elongation at break when compared to injection molding.

Intralayer porosity is responsible for decreased mechanical properties in laser sintered polyamide. Ductility measured in the z-axis is particularly susceptible to the degree of porosity seen between layers and tends to segregate failure modes of specimens into three broad categories: brittle fracture, fracture limited ductility, and full plasticity failure.

Thermally degraded powder does not affect the tensile properties when used in the injection molding process. These degraded powders poor (low) viscosity. Poor viscosity

powders negatively affect the laser sintering process. It is assumed that the high viscosity of thermally degraded powders contribute to poor layer-to-layer adhesion.

Poor layer-to-layer adhesion contributes to the formation of an interface boundary layer. This is evident in both SEM and optical microscopy. Based on the experiments run, it can be concluded that the primary cause of the lower mechanical properties in the z-axis can be attributed to layer-to-layer adhesion and the geometric characteristics of the interface boundary layer.

There are three distinct modes of failure in laser sintered specimens: brittle fracture, fracture limited ductility, and full plasticity failure. It is apparent from the analysis of these samples that the cracks propagate through voids created by a lack of full melt between layers.

The use of an h/r ratio and the relative density of the interface boundary layer help qualify the regions of fracture. An h/r ratio of 0.6 demonstrates a shift between brittle and ductile fracture modes. When the h/r ratio approaches 1.0, there is a major jump in mechanical properties when the interface boundary layer is significantly minimized. This phenomenon may correlate to a unique coplanar shape factor or a critical crack size that instigates fast fracture.

More work is necessary to understand the lack of layer-to-layer adhesion in laser sintered polyamides. Similar materials when molded will have elongation at break (EOB) values of 200-400% while the laser sintered specimens rarely exceed 50%. There is a need to quantify the degree of crystallinity, the existence of micro-cracks or voids that correspond to a critical crack size, the fracture toughness of laser sintered polyamide, and the degree of cross-linking between powder particles in the melt pool. These further studies may allow insight into unique polymer chemistry that will aid in the processing of laser sintering polymers and yield a higher degree of confidence in end-use laser sintered parts.

References

ASM Engineering Materials Handbook. Vol. Plastics.

Caulfield, B, P.E. McHugh, and S Lohfeld. "Dependence of mechanical properties of polyamide components on build parameters in the SLS process." *Journal of Material Processing Technology* (National Centre for Biomedical Engineering Science, Department of Mechanical and Biomedical Engineering, National University of Ireland) 182, no. 2007 (September 2006): 477-488.

CES Edupack, Software. Edited by M. Ashby. Granta Material Intelligence . Granta Design Limited.

Choren, J, V Gervasi, T Herman, S Kamara, and J Mitchell. "SLS Powder Life Study." *SFF Symposium.* Austin, TX: The University of Texas at Austin, 2001. 39-45.

Gornet, T, interview by D.K. Leigh. *Microtoming of Laser Sintering Nylon Specimens* Louisville, KY: University of Louisville, (2010).

Haynes, R. *Powder Metalurgy.* Vol. 20. 1977.

Leigh, D.K., and T Gornet. "Laser Sintering Powder Studies." SLS User's Group, Private Communication.

Majewski, C.E., H Zarringhalam, and N Hopkinson. "Effects of Degree of Particle Melt and crystallinity in SLS Nylon-12 parts." *SFF Symposium.* Austin, TX: The University of Texas at Austin, 2008. 45-54.

Nelson, C, K McAlea, and D Gray. *Improvements in SLS Part Accuracy.* Austin, TX: DTM Corporation, 1995.

Roesler, J, H Harders, and M Baeker. Mechanical Behaviour of Engineering Materials.

Ruffo, M, C Tuck, and R Hague. "Cost estimation for rapid manufacturing - laser sintering production for low to medium volumes." *J. Engineering Manufacture* (Loughborough University) 220 Part B, no. Proc. IMechE (May 2006).

Starr, T, T Gornet, J Usher, and M Sherzer. "Laser Sintering of PA-11 and PA-12 for Direct Digital Manufacturing." *SFF Symposium.* Austin, TX: The University of Texas at Austin, 2008.

Twisp. *Fracture Modes V2.* January 21, 2008. http://en.wikipedia.org/wiki/File:Fracture_modes_v2.svg (accessed 2011).

Yusoff, W.A.Y., and A.J. Thomas. "The effect of employing an effective laser sintering scanning strategy and energy density value on eliminating "orange peel" on a selective laser sintered part." *International Association for Management of Technology.* International Islamic

University Malaysia, Faculty of Manufacturing and Materials Engineering and Innovative Manufacturing Research Centre (IMRC), Cardiff University, Wales, UK, 2008.